Ice shelf basal melt sensitivity to tide-induced mixing based on the theory of subglacial plumes

J. M. Anselin[1,2], B. C. Reed[3], A. Jenkins[4], J. A. M. Green[3]

[1]British Antarctic Survey, UK
[2]Department of Applied Mathematics and Theoretical Physics, University of Cambridge, UK
[3]School of Ocean Sciences, Bangor University, UK
[4]Department of Geography and Environmental Sciences, Northumbria University, UK

Key Points:

- Basal melt sensitivity to tide-induced shear at the ice-ocean interface is evaluated from one-dimensional plume simulations
- The direction of the tide-induced melt response depends on the way in which turbulence created at the ice-ocean interface is assumed to impact entrainment
- The magnitude of the effect of tide-induced mixing is influenced by ambient ocean temperature, ice shelf basal geometry, and tidal current speed

Corresponding author: Mattias Green, m.green@bangor.ac.uk

Abstract

Tidal currents are known to influence basal melting of Antarctic ice shelves through two types of mechanisms: local processes taking place within the boundary current adjacent to the ice shelf-ocean interface and far-field processes influencing the properties of water masses entering the cavity. The separate effects of these processes are poorly understood, limiting our ability to parameterize tide-driven ice shelf-ocean interactions. Here we focus on the small-scale processes within the boundary current and we apply a one-dimensional plume model to a range of ice base geometries characteristic of Antarctic ice shelves to study the sensitivity of basal melt rates to different representations of tide-driven turbulent mixing. Our simulations demonstrate that the direction of the relative change in melt rate due to tides depends on the approach chosen to parameterize entrainment of ambient water into the plume, a process not yet well constrained by observations. A theoretical assessment based on an analogy with tidal bottom boundary layers suggests that tide-driven shear at the ice shelf-ocean interface enhances mixing through the pycnocline. Under this assumption our simulations predict an increase in melt and freeze rates along the base of the ice shelf when adding tides into the model. An approximation is provided to account for this response in basal melt rate parameterizations that neglect the effect of tide-induced turbulent mixing.

Plain Language Summary

Most of Antarctica's coastline is fringed by floating ice platforms called ice shelves. Many ice shelves are thinning through a process called basal melting. This ocean-driven process influences how much the Antarctic Ice Sheet is contributing to global sea level rise. A better understanding of the mechanisms that drive basal melting will therefore help to improve the accuracy of sea level projections. Basal melting is governed by a complex interplay between ocean conditions, ice shelf geometry, and tides. Here we use a one-dimensional computer model to study how currents generated by tides influence basal melting through processes that occur close to the interface between the ice and the ocean. Our model predicts that tidal currents generate an increase in basal melting. However, we also show that the results are sensitive to assumptions made when representing the effects of tides in the computer code. Based on our model results we provide an expression that can be used to estimate the effect of tidal currents on basal melt rates.

1 Introduction

Antarctic ice shelves—the floating tongues of ice that fringe most of the continent's coastline—are formed when glaciers reach the ocean and lose contact with the seabed. Satellite-derived observations have revealed that many ice shelves are experiencing increased thinning, caused primarily by ocean-induced ablation at their base (Jenkins et al., 2018; Paolo et al., 2015). This enhanced level of basal melting reduces the ice shelves' ability to restrain the seaward flow of grounded ice from the interior of the ice sheet (Gudmundsson et al., 2019), resulting in enhanced mass loss—and hence increased sea level rise contribution—from the Antarctic Ice Sheet (AIS). Given the influence of ocean-driven melting on the accelerating rate at which the AIS is contributing to global sea level change (DeConto & Pollard, 2016; Rignot et al., 2019), an improved representation of basal melting in numerical models has become an essential prerequisite for improving the reliability of sea level forecasting.

Ice shelf cavities are often classed as either 'cold' or 'warm' depending on the temperature of the water mass that dominates the sub-ice shelf circulation (Joughin et al., 2012). In cold ice shelf cavities the circulation is driven either by dense high-salinity shelf water (HSSW) formed due to brine rejection from sea ice growth, or by Antarctic Surface Water (AASW). Under warm ice shelves, modified Circumpolar Deep Water (mCDW) comes into contact with the ice base after having intruded onto the continental shelf. In both types of cavities, the release of fresh glacial meltwater into the comparatively saltier ocean leads to the creation of a buoyant meltwater plume that rises up the base of the ice shelf while mixing with ocean water in the cavity. The dynamics of this boundary flow play an important role in regulating the exchange of heat across the ice-ocean interface, which subsequently controls the amount of melting along the base of the ice shelf (Hewitt, 2020). Due to the pressure dependency of the freezing point of seawater, the plume can reach a depth at which it becomes supercooled and forms marine ice, either directly at the ice base or through accretion of suspended frazil ice crystals (Craven et al., 2009; Lambrecht et al., 2007). This sub-ice shelf regime, characterized by melting in the vicinity of the grounding line and ice growth closer to surface, is often referred to as 'ice pump' (Lewis & Perkin, 1986).

Jenkins (1991) numerically described the dynamics of the buoyant flow of ice shelf water in a one-dimensional 'plume model' (schematically represented in Figure 1). Subsequently, several studies have used variations of this framework to provide insight into the physical processes controlling basal melt (e.g. Bombosch & Jenkins, 1995; P. R. Holland & Feltham, 2006; Jenkins, 2011). However, fully resolving the oceanic boundary layer is computationally expensive, which limits the level to which the influence of boundary current dynamics on melt rates can be captured in continental-scale coupled ice-ocean models. In the context of global sea level projections obtained from state-of-the-art ice sheet modelling simulations (e.g. De Boer et al., 2015; DeConto & Pollard, 2016), the influence of basal melt on ice dynamics needs to be modeled without relying on ocean general circulation models. In these instances oceanic forcing can be inferred from more or less complex parameterizations of basal melt rates (Burgard et al., 2022; Favier et al., 2019).

To reduce computational complexity, one oceanic process that is omitted in many ice shelf-ocean models—including the plume model of Jenkins (1991)—and that is hence absent from

parameterizations derived from these models, is the influence of tides (Asay-Davis et al., 2017). However, as described by Padman et al. (2018), tidal currents can affect basal melt through various mechanisms that can be categorized into two types: local processes influencing turbulent mixing within the ice shelf-ocean boundary current, and far-field processes that modulate the thermohaline properties of the water masses coming into contact with the ice base (e.g. sea ice motion, tidal rectification, cavity-scale vertical mixing). Studies based on regional ocean models capable of explicitly simulating tides suggest that the *combined* effect of these processes is to increase the average basal melt rate by 25% to 100% under cold Antarctic ice shelves (Arzeno et al., 2014; Galton-Fenzi et al., 2012; Hausmann et al., 2020; Makinson et al., 2011; Mueller et al., 2012, 2018) and by up to 50% in the case of warm cavities (Jourdain et al., 2019; Robertson, 2013). However, the *separate* effects of each tide-induced mechanism are not as well understood. Addressing this gap in our understanding of the influence of tides would help to develop more effective parameterizations of tide-driven basal melting, which would be a step in the direction toward improved representation of melt rates in numerical models that do not include or resolve tidal currents.

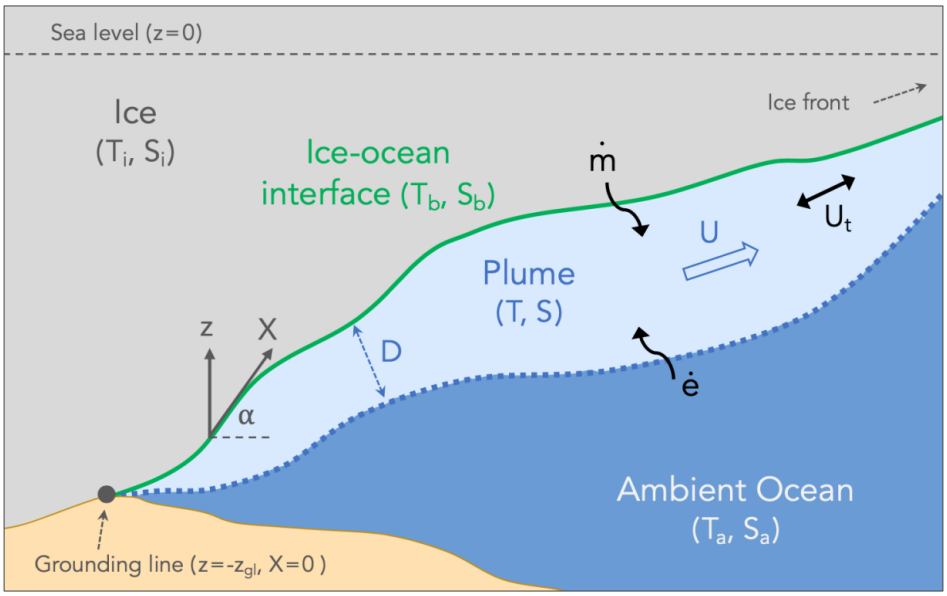

Figure 1. Schematic representation of the one-dimensional plume model of Jenkins (1991) used as basis for this study, and adapted to incorporate the effect of tidal currents U_t. The meltwater plume (colored in light blue and characterized by its thickness D, depth-averaged temperature T, salinity S, and velocity U) is initiated at the grounding line ($z = -z_{gl}, X = 0$) and travels along the base of the ice shelf, following the path X. The geometry of the ice draft along the path of the plume is defined by a local slope $\sin\alpha = dz/dX$. The evolution of the plume is controlled by local entrainment of ambient water ($\dot{e}$) across the pycnocline (represented by the dashed green line) and melting ($\dot{m}$) at the ice-ocean interface (marked in orange). Note that while the seabed has been included in the schematic for illustration purposes, the influence of seabed geometry is ignored in the plume model.

In this study, we focus on local tide-driven turbulent mixing within the boundary current adjacent to the ice shelf-ocean interface, which has been suggested as the dominant mechanism through which tidal currents impact basal melting under Filchner-Ronne ice shelf (Hausmann et al., 2020) and ice shelves in the Amundsen Sea sector (Jourdain et al., 2019). Rather than attempting to quantify absolute basal melt rates, our primary aim is to test the hypothesis that tide-induced turbulence increases basal melt rates under Antarctic ice shelves. To this end, tides are incorporated into the model of Jenkins (1991)—hereafter referred to as 'plume model'—and the model is applied to idealized and realistic ice shelf basal profiles. While there are limitations associated with the use of the plume model (as discussed in section 4), its main advantages are that it is computationally inexpensive while still encapsulating the along-slope boundary current dynamics and its effects on local basal melt rates. Furthermore, one of the most advanced basal melt rate parameterizations for use in standalone ice sheet models, recently developed by Lazeroms et al. (2019) (henceforth abbreviated as L2019), was derived from the same model. If tide-driven turbulent processes are shown to impact basal melt rates, the results from our simulations could potentially be used to improve the L2019 parameterization by accounting for these effects.

This paper is structured as follows: section 2 describes the model set up and gives an overview of the simulations; section 3 presents model results, section 4 highlights model limitations, compares results with findings from previous studies, and discusses considerations for prescribing tide-induced basal melting in ice sheet models; section 5 concludes by suggesting areas for further research.

2 Methods

2.1 Plume model overview

2.1.1 Governing equations without tides

The plume model considers the ocean within the ice shelf cavity as a two-layer system. The top layer (colored in light blue in Figure 1) represents the ice shelf-ocean boundary current, conceptualized here as a buoyant meltwater plume. The plume is characterized in terms of its spatially-varying thickness D, velocity U, temperature T, and salinity S, and it is assumed to be turbulent throughout. The bottom layer (colored in darker blue in Figure 1) represents the ambient ocean, assumed to be stagnant (i.e. the ocean circulation within the cavity is solely driven by the upward motion of the plume). The ice shelf geometry, assumed to be static in time, is described by a local slope $\sin\alpha = dz/dX$, with z being the vertical coordinate and X representing the along-slope distance. The plume is initiated at the grounding line before rising towards the ice front. On its upward path, it grows by entraining ambient ocean water (at rate $\dot{e}$) and it interacts with the ice-ocean interface (characterized by temperature T_b and salinity S_b) either through melting ($\dot{m} > 0$) or through refreezing ($\dot{m} < 0$) depending on the temperature of the plume relative to the local freezing point at the interface. The melt and freeze rates are influenced by turbulent mixing of heat and salt across the plume, parameterized in the model through the heat and salt transfer velocities γ_T and γ_S. The positive buoyancy of the plume is counteracted by ice shelf basal drag, expressed as a function of a constant drag coefficient C_d (refer to Table 1 for model parameter values). Assuming steady-state flow, depth-averaged properties within the

plume, and neglecting Coriolis effects and frazil ice formation gives the following conservation equations for the fluxes of mass, momentum, heat, and salt, respectively:

$$\frac{d(DU)}{dX} = \dot{e} + \dot{m} \tag{1}$$

$$\frac{d(DU^2)}{dX} = D\frac{\Delta\rho}{\rho_0}\, g \sin\alpha - C_d\, U^2 \tag{2}$$

$$\frac{d(DUT)}{dX} = \dot{e}\, T_a + \dot{m}\, T_b - \gamma_T\, (T - T_b) \tag{3}$$

$$\frac{d(DUS)}{dX} = \dot{e}\, S_a + \dot{m}\, S_b - \gamma_S\, (S - S_b) \tag{4}$$

The first term on the right-hand side of equation (2) represents the plume's driving force due to buoyancy. It depends on the dimensionless density difference ($\Delta\rho$) between the plume and the ambient ocean, calculated based on a linear equation of state:

$$\Delta\rho = \frac{\rho_a - \rho_0}{\rho_0} = \beta_S\, (S_a - S) - \beta_T\, (T_a - T) \tag{5}$$

where ρ_0 is a reference density, β_S is the haline contraction coefficient, β_T is the thermal expansion coefficient, ρ_a, T_a and S_a are the ambient ocean density, temperature and salinity, respectively. The entrainment rate $\dot{e}$ is calculated as a linear function of the relative velocity between the boundary layer current and the speed of the surrounding waters. In the original plume framework the ambient ocean is assumed to be motionless, resulting in the following expression:

$$\dot{e} = (E_0 \sin\alpha)\, U \tag{6}$$

with E_0 an empirical constant (Pederson, 1980) and $\sin\alpha$ a factor introduced to account for the effect of slope on entrainment. Three additional equations are required to close the system and solve for $\dot{m}$. They describe the balance of heat and salt fluxes at the ice-ocean interface and constrain the temperature of the ocean in contact with the ice base to be equal to the local depth-dependent freezing point:

$$\gamma_T\, (T - T_b) = \dot{m} \left[\frac{L}{c} + \frac{c_i}{c}\, (T_b - T_i)\right] \tag{7}$$

$$\gamma_S\, (S - S_b) = \dot{m}\, (S_b - S_i) \tag{8}$$

$$T_b = \lambda_1\, S_b + \lambda_2 + \lambda_3\, z_b \tag{9}$$

where L is the latent heat of fusion of ice, c is the specific heat capacity of ocean water, c_i is the specific heat capacity of ice, T_i and S_i are the temperature and salinity of ice, and λ_1, λ_2, λ_3 are empirical constants used to express the seawater freezing point as a function of salinity and depth. The transfer velocities γ_T and γ_S can be expressed as a function of the interfacial friction velocity u_* (D. M. Holland & Jenkins, 1999), defined as the square root of the magnitude of the shear stress τ generated at the interface. The shear stress is commonly formulated in terms of the boundary layer current speed via a quadratic drag law. Within the context of a one-dimensional plume model, this leads to the following friction velocity expression:

$$u_* = \sqrt{\tau} = C_d^{1/2}\, U \tag{10}$$

The heat and salt transfer velocities γ_T and γ_S can then be expressed as a linear function of the plume speed:

$$\gamma_T = \Gamma_T\, u_* = C_d^{1/2}\, \Gamma_T\, U \tag{11}$$

$$\gamma_S = \Gamma_S\, u_* = C_d^{1/2}\, \Gamma_S\, U \tag{12}$$

where Γ_T and Γ_S are the dimensionless turbulent transfer coefficients for heat and salt. Computing $\dot{m}$ based on the above set of equations results in melt rates proportional to the product of the speed and temperature of the plume (Jenkins, 2011).

2.1.2 Tidal parameterization

Here, tidal currents are a source of velocity shear, and hence turbulence, at the ice-ocean interface. We assume that shear-driven turbulent mixing is generated throughout the tidal cycle independent of flow direction and that the root-mean-square (RMS) tidal current speed calculated over a complete tidal cycle, U_t, therefore generates the same amount of turbulent mixing as a steady state oscillating current of the same magnitude. Based on this treatment of tidal velocity, and as recommended by Jenkins et al. (2010), a tidal component was added to the velocity components when calculating the magnitude of the interfacial shear stress. As a result, U was replaced with $\sqrt{U^2 + U_t^2}$ in the transfer velocity formulations, leading to the following modified expressions:

$$\gamma_T = C_d^{1/2}\, \Gamma_T \sqrt{U^2 + U_t^2} \tag{13}$$

$$\gamma_S = C_d^{1/2}\, \Gamma_S \sqrt{U^2 + U_t^2} \tag{14}$$

Similarly, the tide-induced increase in frictional drag at the ice base was incorporated into the model by adding the RMS tidal current to the drag term in equation (2). In line with the formulation implemented by Smedsrud and Jenkins (2004), the conservation equation for momentum then becomes:

$$\frac{d(DU^2)}{dX} = D\Delta\rho\, g \sin\alpha - C_d\, U \sqrt{U^2 + U_t^2} \tag{15}$$

Based on results from tidal model simulations suggesting that tides did not drive mixing beyond the pycnocline (Makinson, 2002), Smedsrud and Jenkins (2004) did not alter the entrainment rate expression when incorporating the effect of tides into their plume model. This approach supports one of the underlying assumptions of the plume model framework, in which entrainment is assumed to be driven solely by shear instability at the outer edge of the plume (and not by the production of turbulent kinetic energy (TKE) at the ice-ocean interface). Assuming tides to be barotropic and the ambient ocean to be static, tidal currents then do not impact the relative velocity between the plume and the ambient ocean and should therefore not be included in the entrainment rate calculation. In contrast, most bulk layer models ignore the dynamical instability of the pycnocline and instead consider sources of TKE at the ice-ocean interface. As a result, ice shelf cavity models that employ

such bulk mixed layer schemes to capture boundary current dynamics (e.g. D. M. Holland & Jenkins, 2001; Little et al., 2009) implicitly assume entrainment to be driven by TKE production at the ice-ocean interface. In this configuration, entrainment is dependent on the absolute speed of the boundary current, which would suggest the following modified entrainment rate formulation (see equation (6) for the original formulation):

$$\dot{e} = (E_0 \sin\alpha) \sqrt{U^2 + U_t^2} \tag{16}$$

Tide forced simulations were performed based on equations (6) and (16) in order to test the sensitivity of tide-induced melt rates to the two contrasting entrainment representations.

Table 1. Constant parameter values applied in this study. The values were selected based on commonly used values (see Table 1 of Hewitt (2020)).

Parameter	Symbol	Value
Entrainment coefficient	E_0	3.6×10^{-2}
Drag coefficient	C_d	2.5×10^{-3}
Thermal Stanton number	$C_d^{1/2}\,\Gamma_T$	1.1×10^{-3}
Haline Stanton number	$C_d^{1/2}\,\Gamma_S$	3.1×10^{-5}
Freezing point salinity coefficient	λ_1	-5.73×10^{-2} °C
Freezing point offset	λ_2	8.32×10^{-2} °C
Freezing point depth coefficient	λ_3	7.61×10^{-4} °C m^{-1}
Thermal expansion coefficient	β_T	3.87×10^{-5} °C^{-1}
Haline contraction coefficient	β_S	7.86×10^{-4} psu^{-1}
Specific heat capacity of ocean water	c	3.974×10^{3} J kg^{-1} °C^{-1}
Specific heat capacity of ice	c_i	2.009×10^{3} J kg^{-1} °C^{-1}
Latent heat of fusion of ice	L	3.35×10^{5} J kg^{-1}
Temperature of ice	T_i	-15 °C
Salinity of ice	S_i	0 psu
Gravitational acceleration	g	9.81 m s^{-2}
Reference seawater density	ρ_0	1030 kg m^{-3}

2.2 Experiments

The model was first applied to idealized, constant slope, ice shelf basal geometries to gain a generalized understanding of the effect of tide-induced turbulence on basal melting. Next, more realistic vertical cross-sections were evaluated to quantify the effect of tides in configurations more representative of Antarctic ice shelves. Table 2 summarizes the model set ups applied in the 'Idealized' and 'Realistic' experiments.

2.2.1 Ice shelf basal geometries

For the Idealized experiment, five basal geometries with constant slope were considered. The grounding line depths and basal slopes for each of these geometries are shown in Table 3 and were defined to encompass the range of values displayed by Antarctic ice shelves, based on the MEaSUREs BedMachine Antarctica dataset (Morlighem et al., 2020). The Realistic experiment runs were conducted for vertical cross-sections along the eight cold cavity flowlines and four warm cavity flowlines shown in Figure 2, with ice shelf boundary

Table 2. Summary of experiments detailing ambient ocean temperature (T_a) and along-path tidal current profile (U_t) applied in each model set up. For tide forced set ups, (tr + dr + e) means that tides were added to the transfer velocity expressions (as per equation (13) and equation (14)), to the plume momentum equation (as per equation (15)) and to the entrainment rate expression (as per equation (16)); (tr + dr) means that tides were added to the transfer velocities and to the plume momentum equation but omitted from the entrainment diagnosis; (tr only) means that tides were only added to the transfer velocities. The tide forced runs in the Realistic experiment were performed by specifying spatially varying RMS tidal current values derived from CATS2008.

Experiment	Identifier	Model set up	T_a	U_t
Idealized	IC0	cold / control	-1.9 °C	zero
	IC1	cold / tide forced (tr only)	-1.9 °C	constant
	IC2	cold / tide forced (tr + dr)	-1.9 °C	constant
	IC3	cold / tide forced (tr + dr + e)	-1.9 °C	constant
	IW0	warm / control	-1.0 °C	zero
	IW1	warm / tide forced (tr only)	-1.0 °C	constant
	IW2	warm / tide forced (tr + dr)	-1.0 °C	constant
	IW3	warm / tide forced (tr + dr + e)	-1.0 °C	constant
Realistic	RC0	cold / control	-1.9 °C	zero
	RC1	cold / tide forced (tr only)	-1.9 °C	spatially varying
	RC2	cold / tide forced (tr + dr)	-1.9 °C	spatially varying
	RC3	cold / tide forced (tr + dr + e)	-1.9 °C	spatially varying
	RW0	warm / control	-1.0 °C	zero
	RW1	warm / tide forced (tr only)	-1.0 °C	spatially varying
	RW2	warm / tide forced (tr + dr)	-1.0 °C	spatially varying
	RW3	warm / tide forced (tr + dr + e)	-1.0 °C	spatially varying

and ice draft topography data again from BedMachine (Morlighem et al., 2020). These flowlines were selected by taking into account ice stream speed and tidal current speeds, and by ensuring that a wide range of Antarctic ice shelf geometries was being considered. Ice drafts were smoothed to reduce noise when computing melt rates.

2.2.2 Ambient ocean conditions

All model runs were performed under uniform ambient ocean conditions by applying constant vertical profiles of temperature and salinity. Cold cavity conditions were simulated with an ambient temperature of $T_a = -1.9\,^{\circ}\mathrm{C}$ which corresponds to the typical temperature of HSSW (Nicholls et al., 2009) and is in line with the thermal forcing applied by most other studies to have investigated the effect of tides on basal melting under cold ice shelves (e.g. Gwyther et al., 2016; Hausmann et al., 2020; Mueller et al., 2018). For warm cavities we used $T_a = -1.0\,^{\circ}\mathrm{C}$, following L2019. In all set ups the ambient salinity was $S_a = 34.65$ psu, again as per the quantity applied by L2019. While in reality salinity varies depending on the water mass ventilating the cavity, we feel that this simplification is justified since salinity has been shown to have limited control on melt rates compared with thermal forcing (P. R. Holland & Jenkins, 2008).

Table 3. Ice shelf basal geometries for which the plume model was evaluated. z_{gl} denotes grounding line depth, z_{if} ice draft at the ice front, and $\overline{\sin\alpha}$ refers to the ice shelf basal slope averaged over the plume path. See Figure 3 and Figure 5 for visual representations of the geometries.

Experiment	Geometries	z_{gl} (m)	z_{if} (m)	Slope	$\overline{\sin\alpha}$
Idealized	Reference	-1000	0	constant	0.002
	Deep	-2500	0	constant	0.002
	Shallow	-500	0	constant	0.002
	Steep	-1000	0	constant	0.01
	Flat	-1000	0	constant	0.001
Realistic	Larsen	-520	-139	varying	0.002
	Talutis (Ronne)	-1273	-122	varying	0.002
	Rutford (Ronne)	-1466	-200	varying	0.002
	Institute (Ronne)	-1002	-258	varying	0.001
	Support Force (Filchner)	-1188	0	varying	0.002
	Amery	-2357	-200	varying	0.004
	MacAyeal (Ross)	-707	-287	varying	0.001
	Mercer (Ross)	-798	-169	varying	0.001
	Thwaites	-571	-58	varying	0.01
	Dotson	-1183	-206	varying	0.01
	Abbot	-353	0	varying	0.004
	Cosgrove	-263	-258	varying	0.0002

2.2.3 Tidal currents

A constant RMS tidal current speed of up to 0.20 m s^{-1} was applied in the tide forced runs of the Idealized experiment. This value corresponds to the upper bound of the flowline-averaged tidal current speed applied to the realistic geometries (see Figure 6). In the Realistic experiment, tide forced simulations were performed by specifying spatially varying tidal current magnitudes along the plume path in order to simulate varying degrees of tide-induced velocity shear at the ice-ocean interface. The RMS tidal current speeds were inferred from the regional barotropic tide model CATS2008 (Circum-Antarctic Tidal Solution version 2008, an update to the model described by Padman et al. (2002)) and calculated as:

$$U_t = \sqrt{\left\langle \left(\frac{U_b}{h}\right)^2 + \left(\frac{V_b}{h}\right)^2 \right\rangle} \tag{17}$$

where U_b and V_b are orthogonal components of depth-integrated volume transport obtained from CATS2008 by accounting for all tidal constituents in the model ($M_2, S_2, N_2, K_2, K_1, O_1, P_1, Q_1, M_f, M_m$), and h is the local water column thickness from BedMachine Antarctica data (Morlighem et al., 2020). The angle brackets mark temporal averaging over a 30-day period (to capture two complete spring-neap cycles and one complete M2-N2 beat cycle).

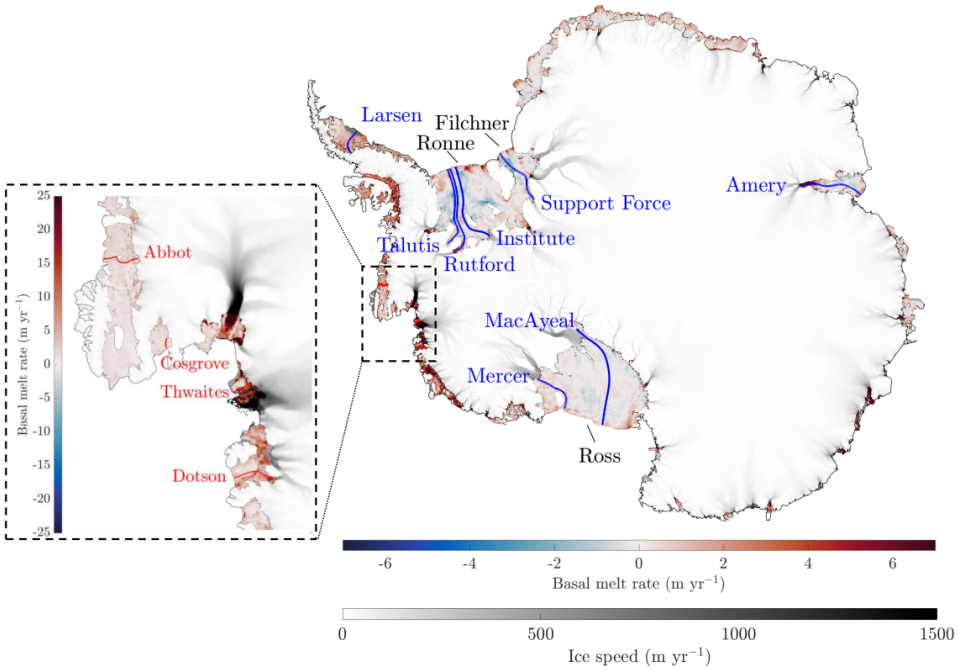

Figure 2. Map showing the Antarctic Ice Sheet (AIS) and plume paths prescribed in the Realistic experiment. The modeled flowlines along cold cavity ice shelves are marked in blue and include Filchner-Ronne ice shelf (Talutis, Rutford, Institute, and Support Force ice streams), Ross ice shelf (Mercer and MacAyeal ice streams), Larsen, and Amery. Modeled warm cavity flowlines are marked in red and include Abbot, Cosgrove, Thwaites, and Dotson. The ice sheet background color indicates ice speed (Mouginot et al., 2012; Rignot et al., 2011) and the ice shelf background color shows basal melt rates derived from 2010-2018 satellite data (Adusumilli et al., 2020).

3 Results

3.1 Model behavior for idealized basal geometries

Adding tides into the model based on the modified formulations of turbulent transfer velocities as per equations (13) and (14), conservation of momentum (15), and entrainment rate (16) acts to speed up the flow of the plume for the idealized reference configuration under both cold and warm conditions (*cf.* solid green lines with dashed-dotted black lines in Figure 3B and 3E, respectively). As expected based on the positive correlation between melt rate and boundary current speed (P. R. Holland & Jenkins, 2008), this translates into increased melt rates (Figure 3C and 3F). In the cold cavity set up, both melting (positive $\dot{m}$ values) and freezing (negative $\dot{m}$ values) increase with the addition of tides. This can be attributed to a strengthening of the ice pump circulation: more melting at depth means more meltwater produced, which decreases the temperature of the plume, thereby decreasing thermal driving, hence increasing the rate of freezing. The increase in melt rate averaged over the melting portion of the plume path is larger than the averaged increase in freeze rate, resulting in a net melt rate increase over the plume path (Figure 4). Under warm cavity conditions no marine ice forms along the plume path. In this melt-only regime, the addition of tides results in an increase in melting at every point along the plume path.

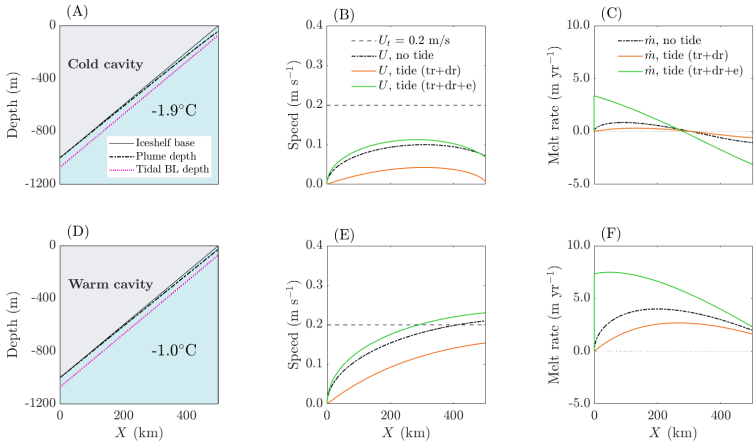

Figure 3. Simulated plume depths and calculated tidal boundary layer depths (A, D), plume speeds (B, E) and basal melt rates (C, F) along the plume path for the constant slope idealized reference geometry under cold ambient conditions (A-C), and warm ambient conditions (D-F). The dash-dotted black lines in B, C, E, and F represent the simulation without tides. The solid orange lines show the results obtained when incorporating tides into the plume model, neglecting the effect of tides on entrainment velocity (simulations IC2 and IW2 in Table 2). The solid green lines were obtained by incorporating the effect of tides into the entrainment expression (IC3 and IW3 in Table 2). All tide-forced results are based on a uniform tidal current speed of 0.20 m s^{-1} specified along the entire plume path (grey dashed lines in B and E). The tidal bottom boundary layer depth was calculated based on equation (18)) with a semi-diurnal tidal frequency.

When incorporating tidal effects into the model without modifying the entrainment scheme (equation (6)), the direction of the tide-induced melt response is reversed. Compared with the simulations without tides, the plume flow speed is now reduced, resulting in a decrease in melt and freeze rates along the plume path (*cf.* solid orange lines with dash-dotted black lines in Figure 3). Regardless of the treatment of entrainment, the melt rate sensitivity to tides is greatest near the grounding zone, where the plume speed without tides (referred to in the following as 'thermohaline-only' plume speed) is lower relative to the applied 0.20 m s^{-1} tidal current speed (dashed grey line in Figure 3B and 3E), as this corresponds to the section of the plume track where tidal currents dominate the flow. Similar behaviours are obtained for the four remaining constant slope geometries (not shown).

Figure 4 illustrates the relative effect of tidal currents on melt rates averaged over the entire plume path, as a function of grounding line depth and basal slope. The blue circles show the results for cold cavity ambient conditions and the red circles represent the warm case, with tide-forced simulations performed with a constant 0.20 m s^{-1} tidal current speed specified along the plume path. Note that the size of the circles relative to each other is more important than their absolute size, as the latter would have varied if a different tidal current magnitude had been applied. Comparing the blue and red circles for each grounding line depth / basal slope combination indicates that the relative effect of tides on melt rates is stronger for cold conditions. This can be attributed to the weaker thermohaline-only plume circulation in the cold regime (*cf.* dash-dotted black line in Figure 3B with dash-dotted

black line in Figure 3E), explained by the positive correlation between boundary current velocity and ambient ocean temperature (P. R. Holland & Jenkins, 2008). The weaker plume flow under cold conditions translates into an increased relative difference between the tidal current speed and plume speed such that the tidal currents are more likely to dominate the flow. Similarly, comparing the thermohaline-only plume speed under a steep ice base with the speed under a flat ice base (not shown) explains why, for the same grounding line depth, the flat ice shelf geometry is more sensitive to tides. Likewise, assuming the same basal slope, the sensitivity to tides decreases as the grounding line depth increases, which again can be explained by considering the difference in thermohaline-only plume speed between both cases.

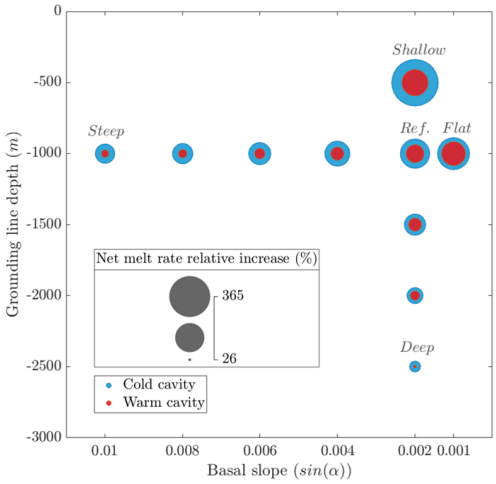

Figure 4. Percentage increase in net melt rate due to tides, calculated as $((\dot{m}_{tideforced} - \dot{m}_{notide})/\dot{m}_{notide}) \times 100$, for different grounding line depth (y-axis) and basal slope (x-axis) configurations. The circle size indicates the magnitude of the relative increase in net melt rate (ranging from 26% for the deep geometry under warm ambient conditions to 365 % for the shallow geometry under cold ambient conditions). Tide forced melt rates were obtained from simulations IC3 and IW3 (Table 2), with a constant 0.20 m s^{-1} tidal current speed specified along the plume path.

3.2 Model behavior for realistic basal geometries

The results obtained for the basal cross-sections along the 12 flowlines presented in Figure 2 are generally in line with trends described for the idealized configurations, i.e. with tidal effects incorporated into the entrainment rate expression the inclusion of tides into the model acts to speed up the plume circulation and increase basal melt rates, and conversely, when the entrainment law is left unchanged, the simulated plume circulation slows down with an associated reduction in basal melt rates. These effects can be seen in the second and third column of Figure 5, for the basal geometries along the flowlines of Talutis ice stream on Ronne ice shelf (cold cavity) and Abbot ice shelf (warm cavity). Although not shown here, the model outputs for the remaining 10 flowlines display similar behaviors.

In contrast to the uniform tidal current applied in the Idealized simulations, spatially dependent tidal current magnitudes were applied along each of the realistic basal geometries

based on data extracted from CATS2008 (see dashed grey lines in Figure 5B and 5E for a visualisation of the tidal current magnitudes applied to the flowlines along Talutis and Abbot). In terms of the resulting along-path variability of tide-induced effects, the influence of tides on circulation strength and melt rates is most pronounced along sections where the tidal current magnitude is largest relative to the thermohaline-only plume speed. The influence of plume path-averaged tidal current speed on melt rate is highlighted in Figure 6, where the flowlines have been presented in descending order based on their flowline-average RMS tidal current magnitude. Consequently, comparing the horizontal position of the green and orange dots in the upper rows of Figure 6B to those in the bottom rows indicates that, irrespective of the treatment of tide-induced entrainment, the effect of tidal currents on basal melt rates appears to be strongest for flowlines experiencing the most intense tides (Filchner-Ronne and Larsen). The effect of tides on melt rates are found to be negligible for flowline-averaged tidal current speeds less than 0.020 m s^{-1} (Amery, Thwaites, Dotson). However, it is worth reiterating that our simulations only capture the shear-driven effect of tides on the ice shelf-ocean boundary current. Therefore, while our model indicates minimal melt rate modulations for some of the flowlines, other tidal mechanisms like for example cavity-scale vertical mixing could hypothetically influence melt rates. It is also clear from Figure 6B that the magnitude of the tide-induced melt rate difference is larger when tides are incorporated into the entrainment rate expression.

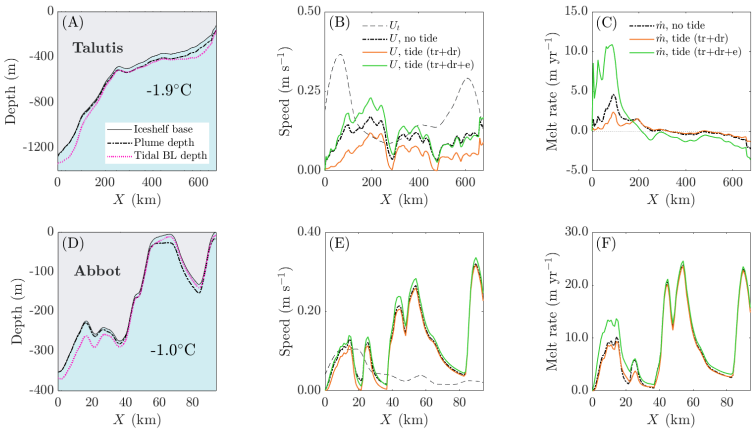

Figure 5. Simulated plume depths and calculated tidal boundary layer depths (A, D), plume speeds (B, E) and basal melt rates (C, F) for two realistic ice base geometries representative of a cold ice shelf (top row, Talutis Ice Stream on Filchner-Ronne ice shelf) and of a warm ice shelf (bottom row, Abbot ice shelf). See Figure 2 for ice shelf locations and Table 3 for basal geometry details. The dash-dotted black lines in B, C, E, and F represent the simulations without tides. The solid orange lines show the results obtained when incorporating tides into the plume model, neglecting the effect of tides on entrainment velocity (simulations RC2 and RW2 in Table 2). The solid green lines were obtained by incorporating the effect of tides into the entrainment expression (RC3 and RW3 in Table 2). The grey dashed line shows the tidal current speed applied along the plume path. The tidal bottom boundary layer depth was calculated as per equation (18)) based on a semi-diurnal tidal frequency.

In addition to the tidal current speed, and as expected based on the findings from the Idealized experiment, ice shelf basal geometry also plays a role in determining the magnitude of tide-induced effects on basal melting. For example, while the local tidal currents applied to Rutford and Institute result in similar flowline-averaged RMS tidal currents speeds (0.14 m s^{-1} for Rutford and 0.13 m s^{-1} for Institute, see Figure 6A), the relative change in flowline-averaged melt rate due to tides is more than 1.4 times larger for Institute. Both flowlines were modeled under the same cold ambient ocean conditions but Institute has a flatter average basal slope (see Table 3). This difference in ice base geometry could explain why Institute is more sensitive to tides, as indicated in Figure 4 in the context of idealized basal geometries where a flatter slope was shown to give rise to a larger relative reduction in melt rate. However, it is important to bear in mind that a linear relationship between melt rate and local basal slope does not always hold (Malyarenko et al., 2020). Therefore, while the results from the Idealized experiment can be used to qualitatively evaluate the sensitivity to tides displayed by different ice shelves, inferring flowline-averaged melt rate based on a flowline-averaged basal slope may not match the value obtained based on the average of locally computed melt rates.

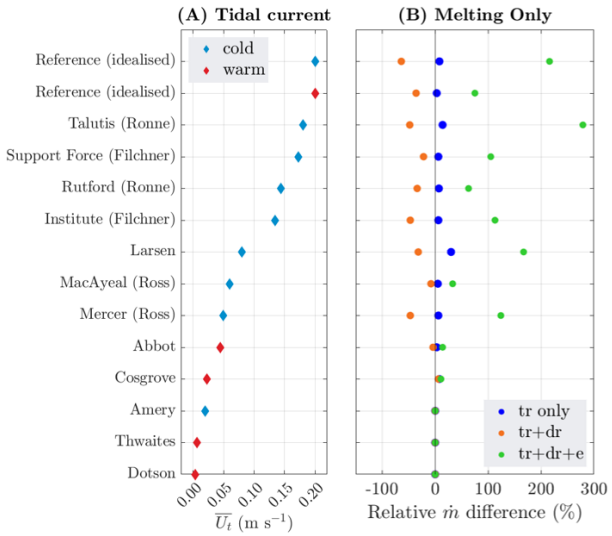

Figure 6. Flowline-averaged RMS tidal current (A) and relative change in basal melt calculated as $(\dot{m}_{tideforced} - \dot{m}_{notide})/\dot{m}_{notide}$ (B) for the idealised constant slope reference geometry, and for the realistic flowline geometries drawn in Figure 2. (B) shows the relative change in $\dot{m}$ for sections along the flowline where $\dot{m}$ is positive (i.e. melting only). Blue dotes in (B) indicate results obtained from model simulations IC1, IW1, RC1, and RW1 (refer to Table 2 for a description of each simulation set up). Orange dots show results from runs IC2, IW2, RC2, and RW2. Green dots were obtained from runs IC3, IW3, RC3, and RW3.

Based on the flowlines considered in this study, cold Antarctic ice shelves appear more sensitive to the effect of tides (Figure 6). This observation holds for the two entrainment related assumptions considered here, and it can be attributed to three main factors. First, some of the largest cold ice shelves around Antarctica are located in regions where tidal

currents happen to be strongest (e.g. Filchner-Ronne and Larsen, see Figure 6A). Secondly, as mentioned in section 3.1, the lower ambient ocean temperature under cold ice shelves leads to slower plume speeds, which results in a larger proportion of the plume path over which tidal currents can dominate the circulation. Thirdly, the flowlines along warm ice shelves like for example Thwaites and Dotson tend to have steeper average basal slopes (see Table 3), which, as suggested by the Idealized experiment results in Figure 4, leads to a lower sensitivity to tide-induced melt rate reductions.

3.3 Evaluation of the entrainment rate formulation in the presence of tides

As shown in Figure 6, incorporating the effect of tides into the model results in either an increase or a decrease in basal melting, depending on the approach chosen to account for the effect of tides on the entrainment process. Leaving the entrainment law unmodified compared to the set up without tides implies that tide-induced shear, and hence turbulence, created at the ice-ocean interface does not drive entrainment. Since the heat source to fuel basal melt comes from entrainment of ambient waters, no additional heat is being supplied to the plume. In this configuration the dominant effect of tide-induced shear is enhanced drag, leading to a plume speed reduction and an associated decrease in steady state melt rate. In contrast, incorporating entrainment driven by TKE production at the ice-ocean interface as per equation (16) results in additional heat available, explaining the observed increase in melt rates. While the former assumption remains in line with the plume framework, the latter is analogous to the approach employed by the majority of bulk mixed layer models in which the rate of entrainment is determined based on an interface stress-driven TKE balance (e.g. Gaspar, 1988). To evaluate which of these two contrasting representations of the entrainment mechanism would be more suitable in the context of this study, we compared the plume thickness (D) obtained from our model simulations without tides with a calculated tidal boundary layer thickness (D_{TBL}). Drawing on an analogy between ice shelf meltwater plumes and tidal bottom boundary layers of shelf seas, and ignoring the effects of Earth rotation and stratification to remain aligned with the plume model set up, D_{TBL} was calculated as (Bowden, 1978):

$$D_{TBL} = \frac{\sqrt{C_d}\, U_t}{\omega} \tag{18}$$

where ω is the tidal frequency. Setting ω to $2\pi/(3600 \times 12.42)$ for locations with dominant semi-diurnal tides and $2\pi/(3600 \times 23.9)$ for diurnal tides and comparing D and D_{TBL} along the plume path for each of the realistic geometries shows that the tidal boundary layer depth exceeds the plume depth along the majority of the ice base. This is illustrated in Figure 5A for Talutis and in Figure 5D for Abbot. Similar results were obtained for the idealized reference geometry under both cold and warm ambient conditions (Figures 3A and 3D). The flowline-averaged values of D_{TBL} exceed the flowline-averaged values of D for most of the flowlines considered in our Realistic experiment (Figure A1). Exceptions to this include ice shelves experiencing very low tidal currents (Dotson, Thwaites, Amery). Bearing in mind that this comparative analysis is based on turbulence theory rather than in-situ observations of the actual physical processes, the findings described above suggest that tidal currents influence mixing beyond the depth of the pycnocline. This supports the incorporation of tides into the entrainment rate expression as per equation (16).

3.4 Quantification of the effect of tide-induced mixing on basal melt rates

The effect of tide-driven turbulent mixing predicted by the plume model was parameterized by deriving an estimate of the tide-induced flowline-averaged melt rate as a function of the ratio between tidal speed and thermohaline-only plume speed. To this purpose, a quadratic regression model was applied to melt rates obtained from the Realistic experiment simulations (Figure 7). The warm cavity flowlines were omitted due to the negligible impact of tides predicted by the plume model for those cases (see Figure 6). An additional data point equal to $(0;0)$ was included to represent the control case without tides. Based on this analysis, the following representation of the effect of tide-driven turbulence on basal melt rate was deduced:

$$\overline{m}_{tideforced} = \begin{cases} \overline{m}_{notide} & \text{(for warm cavities)} \\ \overline{m}_{notide} \times (1 + 0.57\ \overline{U_t}/\overline{U}) & \text{(for cold cavities)} \end{cases} \tag{19}$$

where $\overline{m}_{tideforced}$ is the flowline-averaged melt rate accounting for the effect of tide-induced turbulent mixing, $\overline{m}_{notide}$ is the net melt rate obtained from a model or parameterization that does not incorporate tidal effects (e.g. L2019), $\overline{U_t}$ is the flowline-averaged RMS tidal current speed obtained from a barotropic tide model, and $\overline{U}$ is the flowline-averaged thermohaline-only plume speed. A similar linear relationship was obtained for the idealized set up (Figure B1). As further discussed in section 4, this result must be interpreted carefully due to the limited dataset from which it was derived and due to modeling simplifications (e.g. fixed ambient ocean temperature and salinity applied across all cold cavities), which are deemed acceptable for the purpose of evaluating the relative importance of tide-induced melt, but may restrict our model's capacity to predict absolute basal melt rates.

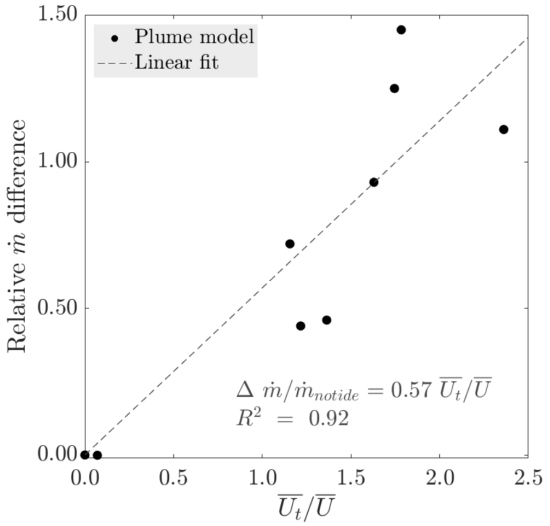

Figure 7. Relative difference in net melt rate due to tides, calculated as $\Delta\ \dot{m}/\dot{m}_{notide} = (\dot{m}_{tideforced} - \dot{m}_{notide})/\dot{m}_{notide}$, versus the ratio of flowline-averaged RMS tidal current speed to flowline-averaged thermohaline-only plume speed for the eight realistic cold cavity flowlines (Figure 2). Tide forced melt rates were obtained from simulations RC3 and RW3 (Table 2).

4 Discussion

4.1 Insights into melt rate sensitivity to tide-induced boundary layer mixing

Based on the assumption that tide-driven shear influences mixing beyond the pycnocline, we have shown that incorporating the effect of tides into a one-dimensional model of ice shelf-ocean boundary current results in an increase in basal melting. The simulated melt rate increase, which can be explained by enhanced transport of heat across the pycnocline, imparts more buoyancy to the plume causing it to accelerate. The increase in plume speed enhances entrainment of ambient water, which decreases the relative importance of tide-induced drag at the ice base. For cold ice shelves, this translates into a strengthening of the ice pump circulation, with amplified melting in the grounding zone, followed by increased freezing further along the plume path. The magnitude of these effects depends on a combination of factors that influence the level to which tidal currents dominate over the thermohaline-only plume circulation (i.e. local tidal current speeds, ambient ocean temperature, ice shelf basal geometry).

It is important to emphasize that these findings are dependent on the approach chosen to incorporate the influence of tides into the model. For the purpose of this study, this consisted of adding an offset equivalent to the RMS tidal current magnitude to the plume speed in the scalar turbulent transfer velocity formulations, momentum flux conservation equation, and entrainment rate expression. The first two modifications parameterize enhanced turbulent mixing of heat, salt, and momentum across the plume caused by turbulence production due to tides at the ice-ocean interface. The increased turbulent transport of heat and salt translates into enhancing the diffusivity of the plume, which, when considered on its own, would result in increased heat flux across the ice-ocean interface and consequently increased melting (see blue dots in Figure 6B). The enhancement of turbulent mixing of momentum creates a counter-effect by increasing the viscosity, which slows down the plume. In the ice shelf configurations considered in this study, with the exception of Cosgrove, the retarding effect of tide-induced drag on the plume dynamics dominates, which would lead to a decrease of heat flux across the ice-ocean interface if entrainment was assumed to be unaffected by tidal currents. Due to the proportionality between melt rate and plume speed this would then translate into a relative reduction in melt rate due to tides (see orange dots in Figure 6B). However, based on a comparative study between the thickness of the simulated plume and a calculated tidal boundary layer thickness, we chose to incorporate amplified entrainment through the pycnocline from tide-induced turbulence created at the ice-ocean interface. In line with P. R. Holland and Feltham (2005), our simulations suggest that the increase in plume speed due to tide-driven turbulent heat transport across the pycnocline dominates over the deceleration due to tide-induced friction at the ice base. As a result, the melt rate increases, causing the boundary current to accelerate, which acts to increase melting further (see green dots in Figure 6B).

Despite the simplified representation of sub-ice shelf ocean dynamics in the 1-D model used here, our results qualitatively agree with those documented in previous 3-D ocean modeling studies, where the explicit inclusion of tidal currents was generally reported to strengthen the cavity circulation and increase rates of basal melting and freezing (e.g. Arzeno et al., 2014;

Gwyther et al., 2016; Makinson et al., 2011; Mueller et al., 2018; Robertson, 2013). However, as previously mentioned, our model only simulates boundary current processes whereas the aforementioned studies also took into account large-scale tidal processes responsible for modifying water masses entering the ice shelf cavity, and hence reported the combined effect of these mechanisms on basal melt. Without the ability to distinguish the influence of the individual tidal processes, it is not possible to establish how the shear-driven effects of tides predicted by our model compare with those simulated by the tide-resolving models mentioned above. By contrast, Jourdain et al. (2019) and Hausmann et al. (2020) applied a decomposition technique to differentiate between changes in basal melt due to boundary current processes and changes induced by tidal mechanisms occurring away from the ice shelf base. Their analyses suggest that tides act to increase net basal melt rates, and that this change is primarily driven by enhanced turbulent heat fluxes at the ice-ocean interface. In line with these results, an increase in melt rates was obtained when adding tides into the plume model based on equations (13-16). However, our analysis suggests that the simulated increase in melt is mainly caused by enhanced turbulent mixing across the outer edge of the plume. While this finding may only be relevant from a qualitative point of view due to the simplicity of our model, it nevertheless highlights the critical importance of the representation of tide-induced mixing across the pycnocline when estimating melt rates in the presence of tidal currents.

While improving the representation of turbulent fluxes at the ice-ocean interface has been the focus of many recent modeling and observational studies (e.g. Dansereau & Losch, 2013; Rosevear et al., 2021), the processes controlling mixing into the boundary current are not yet well understood. For models in which entrainment is unresolved, like the plume model employed in this study, this uncertainty means that the representation of the entrainment process relies on choosing between one of many proposed parameterizations that each vary substantially in terms of predicted entrainment rates (Burchard et al., 2022). More sophisticated 3-D ocean models may not depend on entrainment parameterizations, but they typically employ generic vertical mixing schemes that are not necessarily accurate for the sub-ice shelf environment (Begeman et al., 2022; Jenkins, 2021) and that may respond differently to the addition of tides. This latter point is highlighted by the large range of estimated tide-induced melt rates obtained from 3-D ocean circulation models of the same ice shelf (e.g. Hausmann et al. (2020) and Mueller et al. (2018) for Filchner-Ronne). Both models applied similar parameterizations of heat and salt transfer across the ice-ocean interface but they employed different vertical mixing schemes. Despite other modeling set up differences (e.g. external forcings), this suggests that the variations in simulated tide-driven melt rates can at least partially be attributed to the differing responses of the implemented mixing schemes to the incorporation of tides into the model. The influence that the gaps in our understanding of the entrainment mechanism can have on conclusions drawn from numerical studies supports the need for current measurements across the complete ice shelf-ocean boundary flow and particularly across the pycnocline region.

4.2 Accounting for tide-induced mixing in basal melt rate parameterizations

One of the motivations behind this study was to use the insights gained from the plume model simulations to provide suggestions on how to account for tide-induced basal melt-

ing in standalone ice sheet models that rely on parameterizations to estimate ocean-driven melt. The most accurate approach would be to to follow the analysis presented by L2019 to construct a new melt rate approximation from the plume model equations with modified formulations of the turbulent transfer velocities, plume conservation equation, and entrainment expression as per equations (13-16) to account for the presently neglected effects of tide-induced mixing. However, incorporating an unknown, spatially varying parameter into the analysis would be difficult to implement. A more practical approach would consist in computing melt rates based on the original L2019 expression and then applying an enhancement factor calculated as per the approximation described by equation (19) based on a cavity integrated ratio of tidal current speed to plume speed.

A range of Antarctic ice shelf basal geometries were considered to derive equation (19), and in contrast with most previous studies relying on tidal parameterizations (Asay-Davis et al., 2017), it was obtained by prescribing spatially varying tidal velocities. Nevertheless, it should be applied carefully due to limitations associated with the use of the one-dimensional plume model from which the relationship was derived. More specifically, due to its single horizontal dimension the model does not capture the effects of cross-slope gradients and Earth's rotation, which has been shown to impact the plume flow under large ice shelves (Jenkins, 2011). Secondly, the lack of vertical structure within the plume means that the effect of boundary current stratification on plume dynamics is neglected (Jenkins, 2016) and that parameterized dynamical processes such as entrainment are based on bulk properties of the plume (Burchard et al., 2022). Furthermore, tidal currents are assumed to be barotropic, and the influence of ambient ocean stratification on the plume dynamics—quantified by Bradley et al. (2022)—has been neglected. Finally, as discussed in previous sections, the approximation given in equation (19) is only valid under the assumption that tide-induced shear at the ice-ocean interface impacts mixing beyond the depth of the pycnocline. It should also be noted that, similarly to the standard approach consisting in tuning coefficients to match observed melt rates (e.g. Burgard et al., 2022), applying a melt rate offset based on equation (19) would imply that the relative change in melting due to tides does not vary along the ice base. Since tide-induced melt rates were found to depend on local tidal current strength and local slope, the application of a uniform tide-induced melt rate might bias the prediction of melt rate distribution patterns. However, based on the conclusions of recent study suggesting a minor sensitivity of modeled ice loss to basal melt distribution (Joughin et al., 2021), this bias might be acceptable within the context of ice sheet modeling.

While the approach proposed above might allow for a representation of the effect of tide-induced turbulence on basal melt rates in models that do not resolve tides, parameterizing the effect of tides in this way would imply that tidal currents solely impact melt rates through shear-driven processes within the boundary current. This might be the case under certain ice shelves in the Weddell Sea and Amundsen Sea sectors (Hausmann et al., 2020; Jourdain et al., 2019), but a recent modeling effort based on a pan-Antarctic simulation (Richter et al., 2022) highlighted large regional variations in terms of the mechanisms by which tides modulate basal melt. This emphasizes the importance of applying the tide-induced melt rate parameterization proposed here in conjunction with other parameterizations to account

for basal melt rate modulations introduced by other processes like tidal vertical mixing and residual circulation (e.g. Makinson, 2002).

5 Conclusion

We present a sensitivity analysis of the impact of tide-induced turbulence on ice shelf basal melt rates based on the theory of subglacial plumes. It was performed by incorporating tidal current effects into the one-dimensional model of Jenkins (1991) evaluated with non-stratified ambient ocean conditions, and the results should therefore be interpreted in this context. Our simulations highlight that melt rates depend on the balance between turbulent mixing of heat and momentum across the ice-ocean interface and through the pycnocline (i.e. entrainment). By testing this balance, we have demonstrated that the direction of relative tide-induced basal melt depends on whether tide-driven shear at the ice-ocean interface is assumed to enhance mixing of ambient water into the plume. Based on a limited dataset of 1-D cross-sections along 12 flowlines of Antarctic ice shelves, a linear relationship between tide-induced melt and the ratio of flowline-averaged tidal current magnitude to thermohaline-only plume speed was inferred. In the absence of a new plume parameterization of basal melt incorporating tide-induced mixing effects, this simple approximation could be used in applications in which basal melt rates need to be estimate without relying on ocean general circulation models (e.g. standalone ice sheet models).

Interesting areas of further research that would help to increase the robustness of the proposed parameterization would be to account for the effects of Earth's rotation and boundary current stratification by evaluating the aforementioned tide-induced turbulent mixing processes into a more sophisticated 2-D or 3-D model with sufficient vertical resolution to allow for the meltwater plume to be fully resolved. Finally, while previous observational campaigns have focused on improving the representation of turbulent processes at the ice-ocean interface (e.g. Davis & Nicholls, 2019), there has been less emphasize on quantifying the sources of TKE and their control on entrainment across the pycnocline. While we acknowledge that in-situ current measurements beneath ice shelves are challenging to obtain, given the impact that contrasting theoretical assumptions can have on modeled tide-induced melt rates, obtaining current structure data across the ice shelf-ocean boundary current and beyond the pycnocline in cavities forced by strong tidal currents would be extremely valuable in terms of improving the reliability of Antarctic ice shelf melt rates predictions, and hence sea level rise projections.

Appendix A Comparison between plume thickness and theoretical tidal boundary layer thickness

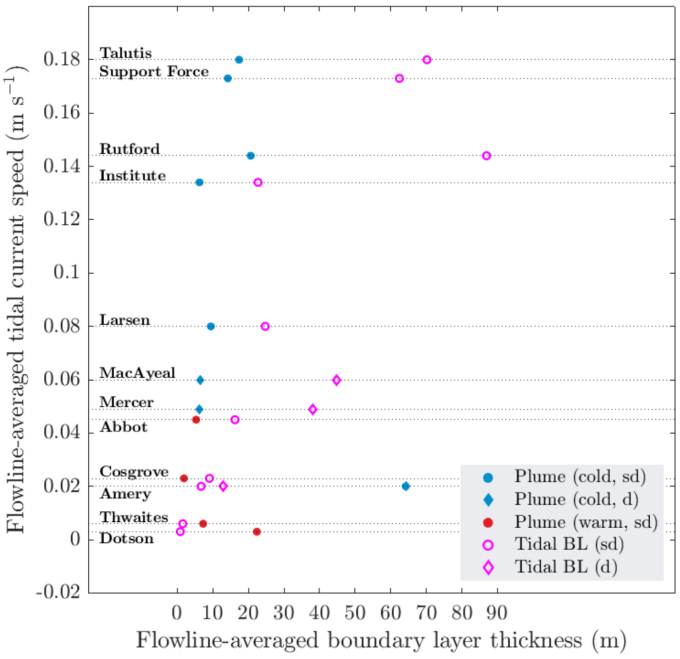

Figure A1. Flowline-averaged plume and tidal boundary layer thickness for the realistic flowlines (Figure 2). Solid markers indicate results obtained from the plume model simulations (blue = cold cavity; red = warm cavity). Pink unfilled markers indicate tidal boundary layer thickness calculated as per equation (18) based on the location specific flowline-averaged tidal current speed (as indicated by the horizontal dashed lines). Circles indicate semi-diurnal tides, diamonds indicate diurnal tides.

Appendix B Regression analysis for idealised geometries

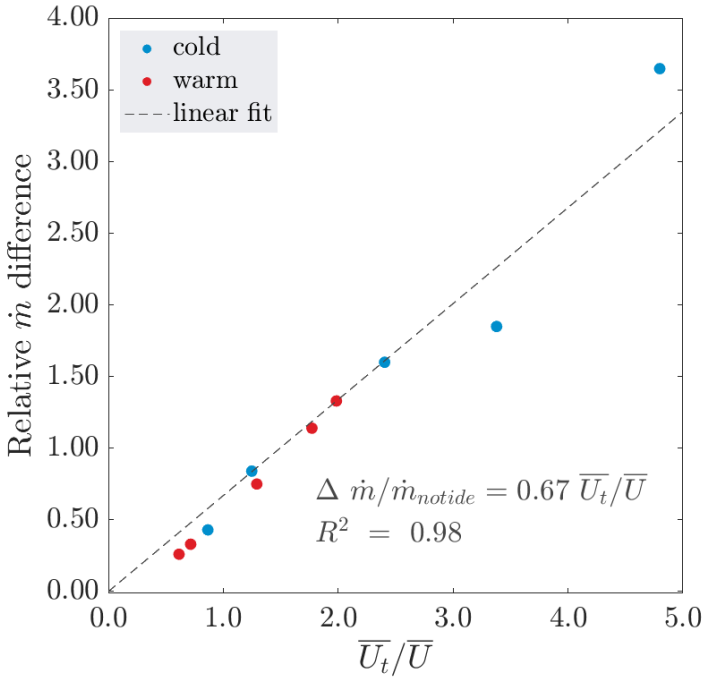

Figure B1. Relative difference in net melt rate due to tides, calculated as $\Delta\ \dot{m}/\dot{m}_{notide} = (\dot{m}_{tideforced} - \dot{m}_{notide})/\dot{m}_{notide}$, versus the ratio of flowline-averaged RMS tidal current speed to flowline-averaged thermohaline-only plume speed for the five idealised geometries (Table 3) under both cold and warm ambient conditions. Tide forced melt rates were obtained from simulations IC3 and IW3 (Table 2).

Appendix C Open Research

The map in Figure 2 was created using the Antarctic Mapping Tools toolbox (Greene et al., 2017) available on Github https://github.com/chadagreene/Antarctic-Mapping-Tools. For the same figure flowline coordinates and ice speed data were obtained from the MEaSUREs InSAR-Based Antarctica Ice Velocity Map, Version 2 dataset (Mouginot et al., 2012; Rignot et al., 2011) available via doi: https://doi.org/10.5067/D7GK8F5J8M8R and basal melt rate data was obtained from Adusumilli et al. (2020) which can be found at https://library.ucsd.edu/dc/object/bb0448974g. Ice shelf profile data (ice base, water column thickness) for the realistic flowlines was obtained from the MEaSUREs BedMachine Antarctic, Version 2 dataset (Morlighem et al., 2020), which can be accessed via doi: https://doi.org/10.5067/E1QL9HFQ7A8M. Tidal current data for the realistic experiment was obtained from the regional barotropic tide model CATS2008 (Circum-Antarctic Tidal Solution version 2.5 2008, an update to the model described by Padman et al. (2002)), available for download through the U.S. Antarctic Program Data Center via doi: 10.15784/601235. The model was accessed using the Tide Model Driver (TMD) version 2.5, Toolbox for Matlab S. Erofeeva, L. Padman, and S. L. Howard (2020) available on Github. Coordinates for the selected flowlines and model outputs used to generate the figures are available at https://github.com/josephineanselin/plumemodeldata.

Acknowledgments

B. C. Reed is supported by an ENVISION Doctoral Training Partnership studentship from the Natural Environment Research Council. J. M. Anselin is supported by a C-CLEAR Doctoral Training Partnership studentship from the Natural Environmental Research Council.

References

Adusumilli, S., Fricker, H. A., Medley, B., Padman, L., & Siegfried, M. R. (2020). Interannual variations in meltwater input to the Southern Ocean from Antarctic ice shelves. *Nature Geoscience*, *13*(9), 616–620. Retrieved from `http://dx.doi.org/10.1038/s41561-020-0616-z` doi: 10.1038/s41561-020-0616-z

Arzeno, I., Beardsley, R. C., Limeburner, R., Owens, B., Padman, L., Spring, S. R., ... Williams, M. J. (2014). Ocean variability contributing to basal melt rate near the ice front of Ross Ice Shelf, Antarctica. *Journal of Geophysical Research: Oceans*, 8410–8421. doi: 10.1002/2014JC009792.Received

Asay-Davis, X. S., Jourdain, N. C., & Nakayama, Y. (2017). Developments in Simulating and Parameterizing Interactions Between the Southern Ocean and the Antarctic Ice Sheet. *Current Climate Change Reports*, *3*(4), 316–329. doi: 10.1007/s40641-017-0071-0

Begeman, C. B., Asay-Davis, X., & Van Roekel, L. (2022, 1). Ice-shelf ocean boundary layer dynamics from large-eddy simulations. *The Cryosphere*, *16*(1), 277–295. doi: 10.5194/tc-16-277-2022

Bombosch, A., & Jenkins, A. (1995). Modeling the formation and deposition of frazil ice beneath Filchner-Ronne Ice Shelf. *Journal of Geophysical Research*, *100*, 6983–6992.

Bowden, K. F. (1978). *Physical problems of the benthic boundary layer* (Tech. Rep.).

Bradley, A. T., Rosie Williams, C., Jenkins, A., & Arthern, R. (2022, 3). Asymptotic analysis of subglacial plumes in stratified environments. *Proceedings of the Royal Society A: Mathematical, Physical and Engineering Sciences*, *478*(2259). doi: 10.1098/rspa.2021.0846

Burchard, H., Bolding, K., Jenkins, A., Losch, M., Reinert, M., & Umlauf, L. (2022, 3). The Vertical Structure and Entrainment of Subglacial Melt Water Plumes. *Journal of Advances in Modeling Earth Systems*, *14*(3). doi: 10.1029/2021ms002925

Burgard, C., Jourdain, N. C., Reese, R., Jenkins, A., & Mathiot, P. (2022). An assessment of basal melt parameterisations for Antarctic ice shelves. Retrieved from `https://doi.org/10.5194/tc-2022-32` doi: 10.5194/tc-2022-32

Craven, M., Allison, I., Fricker, H. A., & Warner, A. R. (2009). Properties of a marine ice layer under the Amery Ice Shelf, East Antarctica. *Journal of Glaciology*, *55*(192), 717–728. doi: 10.3189/002214309789470941

Dansereau, H. P., Veronique, & Losch, M. (2013). Simulation of subice shelf melt rates in a general circulation model: Velocity-dependent transfer and the role of friction. *Journal of Geophysical Research: Oceans*, *2001*(3805), 1–26. doi: 10.1002/2013JC008846.Received

Davis, P. E., & Nicholls, K. W. (2019). Turbulence Observations Beneath Larsen C Ice Shelf, Antarctica. *Journal of Geophysical Research: Oceans*, *124*(8), 5529–5550. doi: 10.1029/2019JC015164

De Boer, B., Dolan, A. M., Bernales, J., Gasson, E., Goelzer, H., Golledge, N. R., ... Van De Wal, R. S. (2015, 5). Simulating the Antarctic ice sheet in the late-Pliocene warm period: PLISMIP-ANT, an ice-sheet model intercomparison project. *Cryosphere*, *9*(3), 881–903. doi: 10.5194/tc-9-881-2015

DeConto, R. M., & Pollard, D. (2016). Contribution of Antarctica to past and future sea-level rise. *Nature*, *531*(7596), 591–597. Retrieved from `http://dx.doi.org/10.1038/`

nature17145 doi: 10.1038/nature17145

Favier, L., Jourdain, N. C., Jenkins, A., Merino, N., Durand, G., Gagliardini, O., ... Mathiot, P. (2019). Assessment of sub-shelf melting parameterisations using the ocean-ice-sheet coupled model NEMO(v3.6)-Elmer/Ice(v8.3). *Geoscientific Model Development*, *12*(6), 2255–2283. doi: 10.5194/gmd-12-2255-2019

Galton-Fenzi, B. K., Hunter, J. R., Coleman, R., Marsland, S. J., & Warner, R. C. (2012). Modeling the basal melting and marine ice accretion of the Amery Ice Shelf. *Journal of Geophysical Research: Oceans*, *117*(9), 1–20. doi: 10.1029/2012JC008214

Gaspar, P. (1988). Modeling the seasonal cycle of the upper ocean. *Journal of Physical Oceanography*, *18*(2), 161–180.

Greene, C. A., Gwyther, D. E., & Blankenship, D. D. (2017, 7). Antarctic Mapping Tools for Matlab. *Computers & Geosciences*, *104*, 151–157. doi: 10.1016/j.cageo.2016.08.003

Gudmundsson, G. H., Paolo, F. S., Adusumilli, S., & Fricker, H. A. (2019). Instantaneous Antarctic ice sheet mass loss driven by thinning ice shelves. *Geophysical Research Letters*, *46*(23), 13903–13909. doi: 10.1029/2019GL085027

Gwyther, D. E., Cougnon, E. A., Galton-Fenzi, B. K., Roberts, J. L., Hunter, J. R., & Dinniman, M. S. (2016). Modelling the response of ice shelf basal melting to different ocean cavity environmental regimes. *Annals of Glaciology*, *57*(73), 131–141. doi: 10.1017/aog.2016.31

Hausmann, U., Sallée, J. B., Jourdain, N. C., Mathiot, P., Rousset, C., Madec, G., ... Hattermann, T. (2020). The Role of Tides in Ocean-Ice Shelf Interactions in the Southwestern Weddell Sea. *Journal of Geophysical Research: Oceans*, *125*(6), 1–29. doi: 10.1029/2019JC015847

Hewitt, I. J. (2020). Subglacial Plumes. *Annual Review of Fluid Mechanics*, *52*, 145–169. doi: 10.1146/annurev-fluid-010719-060252

Holland, D. M., & Jenkins, A. (1999). Modeling thermodynamic ice-ocean interactions at the base of an ice shelf. *Journal of Physical Oceanography*, *29*(8 PART 1), 1787–1800. doi: 10.1175/1520-0485(1999)029⟨1787:mtioia⟩2.0.co;2

Holland, D. M., & Jenkins, A. (2001). Adaptation of an isopycnic coordinate ocean model for the study of circulation beneath Ice Shelves. *Monthly Weather Review*, *129*(8), 1905–1927.

Holland, P. R., & Feltham, D. L. (2005). Frazil dynamics and precipitation in a water column with depth-dependent supercooling. *Journal of Fluid Mechanics*, *530*, 101–124. doi: 10.1017/S002211200400285X

Holland, P. R., & Feltham, D. L. (2006). The effects of rotation and ice shelf topography on frazil-laden ice shelf water plumes. *Journal of Physical Oceanography*, *36*(12), 2312–2327. doi: 10.1175/JPO2970.1

Holland, P. R., & Jenkins, A. (2008). The response of Ice shelf basal melting to variations in ocean temperature. *Journal of Climate*, *21*(11), 2558–2572. doi: 10.1175/2007JCLI1909.1

Jenkins, A. (1991). A One Dimensional Model of Ice-Ocean Interaction. *Journal of Geophysical Research*, *96*(Cll), 671–677.

Jenkins, A. (2011). Convection-driven melting near the grounding lines of ice shelves and tidewater glaciers. *Journal of Physical Oceanography*, *41*(12), 2279–2294. doi:

10.1175/JPO-D-11-03.1

Jenkins, A. (2016). A simple model of the ice shelf-ocean boundary layer and current. *Journal of Physical Oceanography*, *46*(6), 1785–1803. doi: 10.1175/JPO-D-15-0194.1

Jenkins, A. (2021). Shear, Stability and Mixing within the Ice Shelf-Ocean Boundary Current. *Journal of Physical Oceanography*, 2129–2148. doi: 10.1175/jpo-d-20-0096.1

Jenkins, A., Nicholls, K. W., & Corr, H. F. (2010). Observation and parameterization of ablation at the base of Ronne Ice Ahelf, Antarctica. *Journal of Physical Oceanography*, *40*(10), 2298–2312. doi: 10.1175/2010JPO4317.1

Jenkins, A., Shoosmith, D., Dutrieux, P., Jacobs, S., Kim, T. W., Lee, S. H., ... Stammerjohn, S. (2018). West Antarctic Ice Sheet retreat in the Amundsen Sea driven by decadal oceanic variability. *Nature Geoscience*, *11*(10), 733–738. Retrieved from `http://dx.doi.org/10.1038/s41561-018-0207-4` doi: 10.1038/s41561-018-0207-4

Joughin, I., Alley, R. B., & Holland, D. M. (2012). Ice-Sheet Response to Oceanic Forcing. *Science*, *338*(6111), 1172–6. Retrieved from `http://science.sciencemag.org/content/sci/338/6111/1172.full.pdf`

Joughin, I., Shapero, D., Dutrieux, P., & Smith, B. (2021). Ocean-induced melt volume directly paces ice loss from Pine Island Glacier. *Science Advances*, *7*. Retrieved from `https://www.science.org`

Jourdain, N. C., Molines, J. M., Le Sommer, J., Mathiot, P., Chanut, J., de Lavergne, C., & Madec, G. (2019). Simulating or prescribing the influence of tides on the Amundsen Sea ice shelves. *Ocean Modelling*, *133*(October 2018), 44–55. Retrieved from `https://doi.org/10.1016/j.ocemod.2018.11.001` doi: 10.1016/j.ocemod.2018.11.001

Lambrecht, A., Sandhäger, H., Vaughan, D. G., & Mayer, C. (2007, 12). New ice thickness maps of Filchner-Ronne Ice Shelf, Antarctica, with specific focus on grounding lines and marine ice. *Antarctic Science*, *19*(4), 521–532. doi: 10.1017/S0954102007000661

Lazeroms, W. M., Jenkins, A., Rienstra, S. W., & Van De Wal, R. S. (2019). An analytical derivation of ice-shelf basal melt based on the dynamics of meltwater plumes. *Journal of Physical Oceanography*, *49*(4), 917–939. doi: 10.1175/JPO-D-18-0131.1

Lewis, E. L., & Perkin, R. G. (1986). *Ice Pumps and Their Rates* (Vol. 91; Tech. Rep.).

Little, C. M., Gnanadesikan, A., & Oppenheimer, M. (2009). How ice shelf morphology controls basal melting. *Journal of Geophysical Research: Oceans*, *114*(12), 1–15. doi: 10.1029/2008JC005197

Makinson, K. (2002). Modeling tidal current profiles and vertical mixing beneath Filchner-Ronne Ice Shelf, Antarctica. *Journal of Physical Oceanography*, *32*(1), 202–215. doi: 10.1175/1520-0485(2002)032⟨0202:MTCPAV⟩2.0.CO;2

Makinson, K., Holland, P. R., Jenkins, A., Nicholls, K. W., & Holland, D. M. (2011). Influence of tides on melting and freezing beneath Filchner-Ronne Ice Shelf, Antarctica. *Geophysical Research Letters*, *38*(6), 4–9. doi: 10.1029/2010GL046462

Malyarenko, A., Wells, A. J., Langhorne, P. J., Robinson, N. J., Williams, M. J., & Nicholls, K. W. (2020). A synthesis of thermodynamic ablation at ice–ocean interfaces from theory, observations and models. *Ocean Modelling*, *154*(July). doi: 10.1016/j.ocemod.2020.101692

Morlighem, M., Rignot, E., Binder, T., Blankenship, D., Drews, R., Eagles, G., ... Young, D. A. (2020, 2). Deep glacial troughs and stabilizing ridges unveiled beneath the

margins of the Antarctic ice sheet. *Nature Geoscience*, *13*(2), 132–137. doi: 10.1038/s41561-019-0510-8

Mouginot, J., Scheuch, B., & Rignot, E. (2012, 9). Mapping of ice motion in antarctica using synthetic-aperture radar data. *Remote Sensing*, *4*(9), 2753–2767. doi: 10.3390/rs4092753

Mueller, R. D., Hattermann, T., Howard, S. L., & Padman, L. (2018). Tidal influences on a future evolution of the Filchner-Ronne Ice Shelf cavity in the Weddell Sea, Antarctica. *Cryosphere*, *12*(2), 453–476. doi: 10.5194/tc-12-453-2018

Mueller, R. D., Padman, L., Dinniman, M. S., Erofeeva, S. Y., Fricker, H. A., & King, M. A. (2012). Impact of tide-topography interactions on basal melting of Larsen C Ice Shelf, Antarctica. *Journal of Geophysical Research: Oceans*, *117*(5), 1–20. doi: 10.1029/2011JC007263

Nicholls, K. W., Østerhus, S., Makinson, K., Gammelsrød, T., & Fahrbach, E. (2009, 9). *Ice-ocean processes over the continental shelf of the Southern Weddell Sea, Antarctica: A review* (Vol. 47) (No. 3). doi: 10.1029/2007RG000250

Padman, L., Fricker, H. A., Coleman, R., Howard, S., & Erofeeva, L. (2002). A new tide model for the Antarctic ice shelves and seas. *Annals of Glaciology*, *34*, 247–254. doi: 10.3189/172756402781817752

Padman, L., Siegfried, M. R., & Fricker, H. A. (2018). Ocean Tide Influences on the Antarctic and Greenland Ice Sheets. *Reviews of Geophysics*, *56*(1), 142–184. doi: 10.1002/2016RG000546

Paolo, F. S., Fricker, H. A., & Padman, L. (2015). Volume loss from Antarctic ice shelves is accelerating. *Science*, *348*(6232), 327–331. doi: 10.1126/science.aaa0940

Pederson, B. (1980, 8). Dense bottom currents in rotating ocean. *Journal of the Hydraulics Division*, *106*(8).

Richter, O., Gwyther, D. E., King, M. A., & Galton-Fenzi, B. K. (2022, 4). The impact of tides on Antarctic ice shelf melting. *Cryosphere*, *16*(4), 1409–1429. doi: 10.5194/tc-16-1409-2022

Rignot, E., Mouginot, J., & Scheuchl, B. (2011, 9). Ice Flow of the Antarctic Ice Sheet. *Science*, *333*(6048), 1423–1427. doi: 10.1126/science.1207922

Rignot, E., Mouginot, J., Scheuchl, B., Van Den Broeke, M., Van Wessem, M. J., & Morlighem, M. (2019). Four decades of Antarctic ice sheet mass balance from 1979–2017. *Proceedings of the National Academy of Sciences of the United States of America*, *116*(4), 1095–1103. doi: 10.1073/pnas.1812883116

Robertson, R. (2013). Tidally induced increases in melting of Amundsen Sea ice shelves. *Journal of Geophysical Research: Oceans*, *118*(6), 3138–3145. doi: 10.1002/jgrc.20236

Rosevear, M., Galton-Fenzi, B., & Stevens, C. (2021). Evaluation of basal melting parameterisations using in situ ocean and melting observations from the Amery Ice Shelf, East Antarctica. *Ocean Science Discussions*. Retrieved from `https://doi.org/10.5194/os-2021-111` doi: 10.5194/os-2021-111

Smedsrud, L. H., & Jenkins, A. (2004). Frazil ice formation in an ice shelf water plume. *Journal of Geophysical Research: Oceans*, *109*(3), 1–15. doi: 10.1029/2003jc001851